



CHORUS

This is the accepted manuscript made available via CHORUS. The article has been published as:

Instabilities of a rotating helical rod in a viscous fluid

Yunyoung Park, Yongsam Kim, William Ko, and Sookkyung Lim

Phys. Rev. E **95**, 022410 — Published 21 February 2017

DOI: [10.1103/PhysRevE.95.022410](https://doi.org/10.1103/PhysRevE.95.022410)

Instabilities of a rotating helical rod in a viscous fluid

Yunyoung Park and Yongsam Kim*

*Department of Mathematics, Chung-Ang University,
Dongjakgu, Heukseokdong, Seoul, 156-756, Republic of Korea.*

William Ko and Sookkyung Lim†

*Department of Mathematical Sciences, University of Cincinnati,
4199 French Hall West, Cincinnati, OH 45221, USA*

Abstract

Bacteria such as *Vibrio alginolyticus* swim through a fluid by utilizing the rotational motion of their helical flagellum driven by a rotary motor. The flagellar motor is embedded in the cell body and turns either clockwise (CW) or counterclockwise (CCW), which may lead to straight forward or backward swimming, or reorientation of the cell. In this paper we investigate the dynamics of the helical flagellum by adopting the Kirchhoff rod theory in which the flagellum is described as a space curve associated with orthonormal triads that measure the degree of bending and twisting of the rod. The hydrodynamic interaction with the flagellum is described by the regularized Stokes formulation. We focus on two different types of instabilities; (1) whirling instability of a rotating helical filament in the absence of a hook and (2) buckling instability of a flagellum in the presence of a compliant hook that links the flagellar filament to the rotary motor. Our simulation results show that the helical filament without a hook displays three regimes of dynamical motions; stable twirling, unstable whirling, and stable overwhirling motions depending on the physical parameters such as rotational frequency and elastic properties of the flagellum. The helical filament with a hook experiences buckling instability when the motor switches the direction of rotation and the elastic properties of the hook change. Variations of physical parameter values of the hook such as the bending modulus and the length make an impact on the buckling angle which may subsequently affect the reorientation of the cell.

* Co-corresponding author. kimy@cau.ac.kr

† Co-corresponding author. sookkyung.lim@uc.edu

I. INTRODUCTION

Monotrichous bacteria such as *V. alginolyticus* swim through a fluid by rotating their helical flagellum. The rotational motion of the flagellum is driven by a rotary motor which is embedded in the cell body and connected to the flagellar filament through a hook. The motor and the flagellum turn together either clockwise (CW) or counterclockwise (CCW), which leads to straight forward or backward swimming, or the reorientation of bacteria [1–3]. Here we investigate the dynamics of a helical flagellum in which the motor is anchored in space and rotates at a given frequency. We consider two different types of instabilities: (1) whirling instability of a rotating helical flagellum in the absence of a hook, and (2) buckling instability of a rotating helical rod in the presence of a compliant hook which links the helical filament to the rotary motor. The hook is much more flexible than the flagellar filament, and its length is substantially shorter than the length of the filament.

Wolgemuth *et al.* [4] studied the whirling instability of a rotating elastic rod that is intrinsically straight and immersed in a Stokes flow by using slender body theory. They found a critical rotating frequency that classifies the dynamical motions of the rod into two categories; whirling and twirling. Lim *et al.* [5] and Lee *et al.* [6] further classified the dynamical steady states into three different regimes; twirling, whirling, and overwhirling. Twirling is a stable motion in which the elastic rod returns to a straight state and rotates at a constant speed. Whirling is an unstable motion in which the rod tilts slightly away from the rotational axis with a certain angle, but continues to rotate about the rotational axis. Overwhirling is a stable motion in which the rod bends with a large amplitude and rotates at a constant speed. They found that twirling and overwhirling coexist as stable dynamical states at subcritical spinning frequencies, which was also observed in Manghi *et al.* [7] and Wada and Netz [8].

In this paper, we investigate the dynamics of a rotating elastic rod that is intrinsically a left-handed helix and immersed in a Stokes fluid. The motor end of the rod is tethered in space but is able to rotate at a prescribed frequency, whereas the other end is free to move around in the fluid. As in the case of the intrinsically straight rod, we find from our simulation results that a rotating helical rod also exhibits three dynamical regimes while the rod keeps its helical shape. It is also observed that the critical frequencies for the transition between the three regimes change as we vary the physical parameters such as the elastic and geometric properties of the rod and the fluid viscosity.

Son *et al.* [3] discovered that the monotrichous bacterium *V. alginolyticus* flicks when there occurs a buckling instability of the hook. Buckling of the hook plays a significant role in determining the swimming pattern and the chemotaxis of single-flagellated bacteria [3, 9]. *V. alginolyticus* swims backward by turning the motor CW while the hook is under tension. Then it suddenly changes the rotational direction of the motor to CCW, which causes the bacterium to swim forward and its hook to be in a compressed state. The onset of compression of the hook may trigger the buckling instability of the flagellum followed by the flicks of the bacterium. The length of the hook is about 100 nm [10] which is very short compared to that of the helical filament (4-5 μm). The bending modulus of the hook is 2-3 orders of magnitude smaller than that of the helical filament, and thus the hook can be easily bent. For more detailed information on the role of the hook in the swimming process of bacteria, the reader may refer to the experimental and theoretical works in [3, 11, 12].

Here we model a hook as an intrinsically straight rod and connect it to the helical flagellum at one end and to the rotary motor at the other end. Then we change the rotational direction of the motor from CW to CCW to investigate the buckling instability of the flagellum which may subsequently affect the reorientation of the cell. We vary the physical parameters of the hook such as the bending and twist moduli and the length of the hook to explore how these parameters affect the buckling angle which is defined as the angle between the rotational axis and the helical axis. We shall see that the buckling angle depends substantially on the bending modulus and the length of the hook, but is independent of the twist modulus.

In order to investigate the fluid-mechanical interaction of the helical flagellum regarding two different types of instabilities, we use the regularized formulation [13] for a Stokes flow combined with the unconstrained Kirchhoff rod theory for an elastic rod. This method was first developed by Olson *et al.* [6, 14] in which the elastic rod is represented by a space curve together with orthonormal triads that measure the amount of bending and twisting along the rod. The small length scales associated with bacterial motility permit the use of Stokes flow in which the inertial effects are ignored just as in a very low Reynolds number flow. The elastic rod applies force and torque to the fluid and moves at the local fluid velocity while the triads rotate at the local angular fluid velocity obtained by the regularized fundamental solution of the Stokes flow.

II. MATHEMATICAL MODEL

We use the Kirchhoff rod theory to model a helical flagellum of bacteria such as *V. alginolyticus*, see Fig. 1 for a schematic diagram of our computational model. Kirchhoff rod theory uses a space curve $\mathbf{X}(s, t)$ to describe the centerline of the flagellum and an associated orthonormal triad $\{\mathbf{D}^1(s, t), \mathbf{D}^2(s, t), \mathbf{D}^3(s, t)\}$ to represent the amount of bending and twisting of the flagellum. Here, t is time and s is a Lagrangian coordinate along the rod with $0 \leq s \leq L_h + L_f$, where L_h and L_f are the lengths of the hook and the helical flagellar filament, respectively. The initial shape of the helical centerline $\mathbf{X}(s, 0)$ is described as follows [15]:

$$\mathbf{X}(s, 0) = (r(s) \cos(\alpha s), r(s) \sin(\alpha s), s), \quad (1)$$

where α is the wave number and the helical radius $r(s)$ is a variable function defined as

$$r(s) = \begin{cases} 0 & , \quad 0 \leq s \leq L_h \\ r_0 \left(1 - e^{-q(s-L_h)^2}\right) & , \quad L_h \leq s \leq L_h + L_f. \end{cases} \quad (2)$$

The helical radius is 0 for the hook ($0 \leq s \leq L_h$) which is a straight rod, and then increases gradually to be r_0 for the helical flagellar filament ($L_h \leq s \leq L_h + L_f$), see Fig. 1.

The vector $\mathbf{D}^3(s, t)$ is initially defined as a unit tangent vector to the helical flagellum in (1), and the other two vectors, $\mathbf{D}^1(s, t)$ and $\mathbf{D}^2(s, t)$, are perpendicular to the tangent vector following the right-hand rule, i.e., normal and binormal vectors to the flagellum. Note that this initial configuration of the centerline and the triad of the helical flagellum is in the equilibrium state in the absence of external forces, and that their deformation gives rise to the internal energy and force.

Now we equip the bottom end of the hook with a rotary motor. The motor point is tethered in space at $\mathbf{X}_{\text{mot}} = \mathbf{X}(0, 0)$ and turns either CW or CCW at a prescribed angular frequency ω . This can be done by defining the orthonormal triad of the motor point as follows:

$$\mathbf{D}_{\text{mot}}^1(t) = (\cos(2\pi\omega t), -\sin(2\pi\omega t), 0), \quad (3)$$

$$\mathbf{D}_{\text{mot}}^2(t) = (\sin(2\pi\omega t), \cos(2\pi\omega t), 0), \quad (4)$$

$$\mathbf{D}_{\text{mot}}^3(t) = (0, 0, 1), \quad (5)$$

where t is the time in seconds and ω is the rotation rate in Hz. The sign of ω determines the direction of rotation, i.e., $\omega > 0$ corresponds to CCW rotation and $\omega < 0$ corresponds to CW rotation when the rod is viewed towards the motor from the helical filament. The rotation of the motor applies the torque to the helical flagellum through the straight hook which may also rotate.

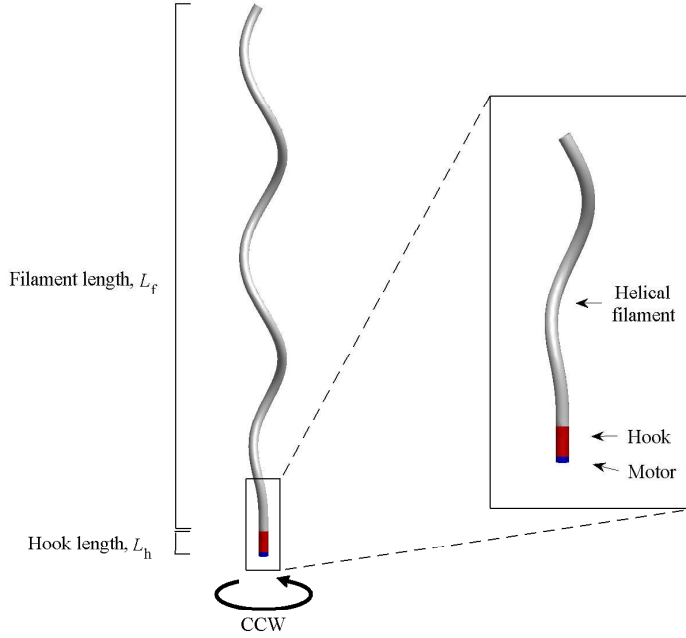


FIG. 1. (Color online) A schematic view of a computational model for a left-handed helical flagellum. The helical flagellar filament is linked to a compliant hook which is linked to a rotary motor that is tethered in space and turns either counterclockwise (CCW) or clockwise (CW). The motor is represented by a single material point.

Let $\mathbf{N}(s, t)$ and $\mathbf{F}(s, t)$ be the moment and the force, respectively, which are transmitted across a section of the rod at the Lagrangian coordinate s at time t . Let $\mathbf{f}(s, t)$ and $\mathbf{n}(s, t)$ be the applied force and the torque densities, respectively. Then the momentum and angular momentum balance equations are described as follows:

$$0 = \mathbf{f} + \frac{\partial \mathbf{F}}{\partial s}, \quad (6)$$

$$0 = \mathbf{n} + \frac{\partial \mathbf{N}}{\partial s} + \left(\frac{\partial \mathbf{X}}{\partial s} \times \mathbf{F} \right), \quad (7)$$

where all the variables may be expanded in the basis of the orthonormal triad as follows:

$$\mathbf{F} = \sum_{i=1}^3 F_i \mathbf{D}^i, \quad \mathbf{N} = \sum_{i=1}^3 N_i \mathbf{D}^i, \quad \mathbf{f} = \sum_{i=1}^3 f_i \mathbf{D}^i, \quad \text{and} \quad \mathbf{n} = \sum_{i=1}^3 n_i \mathbf{D}^i. \quad (8)$$

The constitutive relations are given by

$$N_i = a_i \left(\frac{\partial \mathbf{D}^j}{\partial s} \cdot \mathbf{D}^k - \Omega_i \right), \quad (9)$$

where (i, j, k) is any cyclic permutation of $(1, 2, 3)$, and

$$F_i = b_i \left(\mathbf{D}^i \cdot \frac{\partial \mathbf{X}}{\partial s} - \delta_{3i} \right), i = 1, 2, 3, \quad (10)$$

where δ_{3i} is the Kronecker delta. The coefficients a_1 and a_2 are the bending moduli, and a_3 is the twist modulus of the rod. The coefficients b_1 and b_2 are the shear moduli, and b_3 is the stretching modulus which controls the degree of the inextensibility of the rod. The strain twist vector $\boldsymbol{\Omega} = (\Omega_1, \Omega_2, \Omega_3)$ designates the intrinsic property of the elastic rod in which $\kappa \equiv \sqrt{\Omega_1^2 + \Omega_2^2}$ is the intrinsic curvature and Ω_3 is the intrinsic twist of the rod of which the sign determines the helical handedness of the rod. A negative value of Ω_3 corresponds to a left-handed helix and a positive value of Ω_3 corresponds to a right-handed helix. We assume that the helical rod is intrinsically left-handed throughout this work. The constitutive relations above can be derived from a variational argument of the elastic energy potential for the unconstrained version of the Kirchhoff rod

$$E = \frac{1}{2} \int_0^L \left[a_1 \left(\frac{\partial \mathbf{D}^2}{\partial s} \cdot \mathbf{D}^3 - \Omega_1 \right)^2 + a_2 \left(\frac{\partial \mathbf{D}^3}{\partial s} \cdot \mathbf{D}^1 - \Omega_2 \right)^2 + a_3 \left(\frac{\partial \mathbf{D}^1}{\partial s} \cdot \mathbf{D}^2 - \Omega_3 \right)^2 + b_1 \left(\mathbf{D}^1 \cdot \frac{\partial \mathbf{X}}{\partial s} \right)^2 + b_2 \left(\mathbf{D}^2 \cdot \frac{\partial \mathbf{X}}{\partial s} \right)^2 + b_3 \left(\mathbf{D}^3 \cdot \frac{\partial \mathbf{X}}{\partial s} - 1 \right)^2 \right] ds, \quad (11)$$

where $L = L_h + L_f$ is the total length of the rod. Note that, in the limit $b_3 \rightarrow \infty$, the rod becomes completely inextensible. In this work, we choose the value of b_3 sufficiently large to make the rod almost inextensible and set $a_1 = a_2$ which implies that the rod is isotropic.

The helical rod is immersed in a viscous fluid which is governed by the incompressible regularized Stokes equations

$$0 = -\nabla p + \mu \Delta \mathbf{u} + \mathbf{g}, \quad (12)$$

$$0 = \nabla \cdot \mathbf{u}, \quad (13)$$

where μ is the fluid viscosity. The unknown variables \mathbf{u} , p , and \mathbf{g} are the fluid velocity, pressure, and the external force per unit volume applied to the fluid, respectively, and they are functions of the fixed Cartesian coordinates \mathbf{x} and the time t . The fluid force density \mathbf{g} in Eq. (12) is given by

$$\mathbf{g}(\mathbf{x}, t) = \int_0^L (-\mathbf{f}(s, t)) \psi_\epsilon(\mathbf{x} - \mathbf{X}(s, t)) ds + \frac{1}{2} \nabla \times \int_0^L (-\mathbf{n}(s, t)) \psi_\epsilon(\mathbf{x} - \mathbf{X}(s, t)) ds, \quad (14)$$

where the radially symmetric blob function ψ_ϵ is defined as

$$\psi_\epsilon(\mathbf{r}) = \frac{15\epsilon^4}{8\pi(|\mathbf{r}|^2 + \epsilon^2)^{7/2}}, \quad (15)$$

where ϵ is the regularization parameter and $\mathbf{r} = \mathbf{x} - \mathbf{X}$ for a point \mathbf{x} in the fluid [13, 14]. The blob function ψ_ϵ is a bell-shaped function with infinite support and satisfies $\iiint_{\mathbf{R}^3} \psi_\epsilon(\mathbf{r}) d\mathbf{r} = 1$, spreading most of the force and moment within a ball with the radius ϵ and the center at the rod \mathbf{X} . Eq. (14) describes how we apply the force and torque generated in the rod to the fluid, and this implies that the rate at which the elastic rod works on the fluid is written in terms of the force and moment applied to the fluid by the rod [16].

Together with Eqs. (6)-(10) and (12)-(14), the coupled system of equations closes with the addition of the following equations:

$$\mathbf{w}(\mathbf{x}, t) = \frac{1}{2} \nabla \times \mathbf{u}(\mathbf{x}, t), \quad (16)$$

$$\frac{\partial \mathbf{X}(s, t)}{\partial t} = \mathbf{u}(\mathbf{X}(s, t), t), \quad (17)$$

$$\frac{\partial \mathbf{D}^i(s, t)}{\partial t} = \mathbf{w}(\mathbf{X}(s, t), t) \times \mathbf{D}^i(s, t), i = 1, 2, 3. \quad (18)$$

Eq. (16) is the relation between the fluid angular velocity \mathbf{w} and the fluid velocity \mathbf{u} , both of which are solved using a regularized Stokes formulation. The interaction between the elastic rod and the fluid is described in Eqs. (17) and (18) which are the no-slip conditions for the velocity and the angular velocity, respectively. These equations imply that the centerline of the rod translates at the local fluid velocity and that the triad rotates at the local fluid angular velocity. The numerical method we used here is a grid-free Lagrangian method for thin filamentous structures that capture the bend and twist of an elastic rod at zero Reynolds number. The local linear and angular velocities are represented as a superposition of regularized fundamental solutions and hence we only need to evaluate the linear and angular velocities at the centerline of the elastic rod. See [6, 14] for a more detailed description of both mathematical formulation and its numerical scheme.

Table I shows the computational and physical parameters used in this paper. The fluid viscosity μ is the same as that of water. We compute the intrinsic strain vector $\boldsymbol{\Omega} = (\Omega_1, \Omega_2, \Omega_3)$ from the initial shape of the helical filament given in Eqs. (1) and (2). Since the radius of the helical filament increases continuously from 0 to r_0 , the intrinsic strain vector is also a variable function. The intrinsic curvature $\kappa = \sqrt{\Omega_1^2 + \Omega_2^2}$ and twist Ω_3 given in Table I are the values of the helical filament with a constant radius r_0 . Note that we use the exponent $k = 2$ in Eq. (2) and therefore the majority of our filament model has approximately a constant helical radius r_0 . In the following

TABLE I. *Computational and physical parameters*

Parameters (symbol)	Value
Fluid viscosity (μ)	$0.01 \times 10^{-4} \text{ g}/(\mu\text{ms})$
Meshwidth for flagellum (Δs)	$0.03125 \mu\text{m}$
Number of material points of the rod	149
Regularization parameter (ϵ)	$5\Delta s$
Time step (Δt)	$3 \times 10^{-8} \text{ s}$
Helical radius of filament (r_0)	$0.14 \mu\text{m}$
Length of filament (L_f)	$4.5 \mu\text{m}$
Intrinsic curvature of filament (κ)	$1.8461 \mu\text{m}^{-1}$
Intrinsic twist of filament (Ω_3)	$3.1270 \mu\text{m}^{-1}$
Bending modulus of filament ($a_1 = a_2 = a$)	$0.05 \text{ g}\mu\text{m}^3/\text{s}^2$
Twist modulus of filament (a_3)	$0.05 \text{ g}\mu\text{m}^3/\text{s}^2$
Shear modulus ($b_1 = b_2$)	$2.0 \text{ g}\mu\text{m}/\text{s}^2$
Stretch modulus (b_3)	$2.0 \text{ g}\mu\text{m}/\text{s}^2$
Length of hook (L_h)	$0.0938 \mu\text{m}$
Bending modulus of relaxed hook (a_{relax})	$0.0001-0.0008 \text{ g}\mu\text{m}^3/\text{s}^2$
Bending modulus of loaded hook (a_{load})	$0.0006-0.0012 \text{ g}\mu\text{m}^3/\text{s}^2$
Twist modulus of hook (a_3^{hook})	$(0.1-1) \times a_3 \text{ g}\mu\text{m}^3/\text{s}^2$

section, we investigate how the physical parameters pertaining to the filament and the fluid affect the dynamics of a rotating rod.

III. RESULTS AND DISCUSSION

A. Whirling instability of a rotating helix with no hook

The helical filament is equipped with a motor which is fixed at the bottom end of the filament and rotates at a prescribed angular frequency. The twist generated by the rotary motor is being transmitted along the filament and reaches its free end which leads to the rotation of the whole helical filament. In this section, we investigate the whirling instability of a rotating helical filament

in the absence of the hook. As in the previous studies in [4–6] where the rotating rod is intrinsically straight, we observe three different dynamical states as the rotational frequency varies between separate simulations. When the motor rotates at low speed, the helical rod spins about its rotational axis which remains straight. This is called a stable *twirling* motion. As the rotational frequency increases, the standing helical filament becomes unstable, and it bends below the motor point and rotates steadily with a large amplitude, which is referred to as a stable *overwhirling* state. The unstable steady motion in between is called a *whirling* state.

Fig. 2 shows two stable dynamical motions of a rotating helical filament that is initially tilted away from the axis of rotation. The filament is intrinsically helical and reaches either a stable twirling (top) or a stable overwhirling (bottom) when the rotational frequency is given as 1400 Hz and 1500 Hz, respectively. This suggests that there exists a critical frequency ω_c that separates overwhirling from twirling. When the angular frequency ω is lower than the critical frequency ω_c , the helical filament rotates and is relaxed to a stable twirling motion. However, at a higher frequency, $\omega > \omega_c$, the helical filament of which the axis is straight becomes unstable and gets to a stable overwhirling state. Note that, depending on whether the rotational motor frequency is far from or close to the critical frequency, it determines how fast the helical rod reaches either stable twirling state or stable overwhirling state and also determines the rotational speed, called crankshafting frequency, of the rod as a whole.

When the rod is intrinsically straight and rotates with a small initial perturbation, Wolgemuth *et al.* [4] derived the following relation between the critical frequency and various physical parameters using the weakly nonlinear theory

$$\omega_c \sim \frac{4}{\pi} \left(\frac{1}{RL} \right)^2 \frac{a}{\mu}, \quad (19)$$

where R is the thickness of the rod, L is the length of the rod, μ is the fluid viscosity, and a is the bending modulus. Our simulation results show that the critical frequency that distinguishes overwhirling from twirling depends on the physical properties of the helical filament and the surrounding fluid in the same fashion as predicted by the theory in [4], even though our model filament is intrinsically helical whereas the filament in [4] is intrinsically straight.

Fig. 3 shows the dynamical state of the rotational filament when we change the rotational frequency and one of four different parameters; the bending modulus (upper-left), twist modulus (upper-right), fluid viscosity (lower-left), and the length of the flagellar filament (lower-right). When one of the parameters varies, all the other parameter values are held fixed. The x -axis and

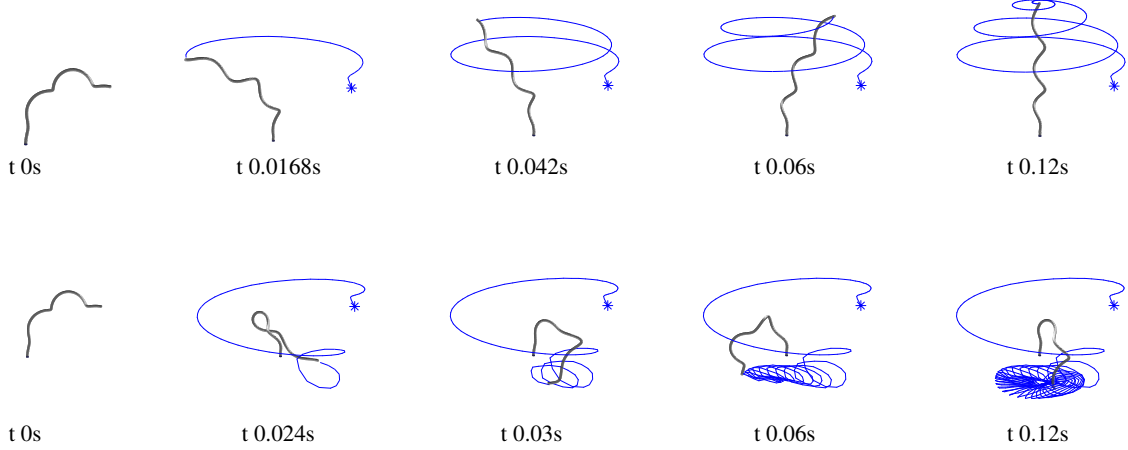


FIG. 2. (Color online) Time evolution of two stable dynamical motions of a rotating helical filament with the path (blue) traced out by the free end. The filament is intrinsically helical and the initial configuration is tilted away from the axis of rotation. The filament reaches either a stable twirling (top) or a stable overwhirling (bottom) when the rotational frequency is given as 1400 Hz and 1500 Hz, respectively. The motor turns CCW in both cases.

y -axis represent one of the physical parameters and the angular frequency of the motor, respectively. The red circles denote the stable overwhirling state, and blue crosses denote the stable twirling state. The figure demonstrates that there exists a critical frequency of the motor, below which the filament approaches a stable twirling state, but above which the filament stabilizes in the overwhirling state. The dashed lines indicate the best fit of the critical frequency ω_c to a function of the form $y = cx^m$, where c is a constant and m is the order of the power function and they are determined by using the least square approximations. We can see from Fig. 3 that the critical frequency is linearly dependent on the bending modulus a (a), independent of the twist modulus a_3 (b), inversely proportional to the fluid viscosity μ (c), and inversely proportional to the square of filament length L_f (d), which are consistent with the relation in Eq. (19) for the case of an intrinsically straight rod. Specifically, we obtain $m \sim 0.9472$ in (a), $m \sim 0$ in (b), $m \sim -0.9994$ in (c), and $m \sim -2.0536$ in (d).

We also vary the radius r_0 of the helical filament to investigate the dependence of the critical frequency on the helical geometry. Fig. 4 shows the dynamical states of the rotating filament for various rotational frequencies ω and helical radii r_0 . Here, we fix the helical pitch at $2\pi p$ with $p = 1.5 \mu\text{m}$ and the twist modulus at $a_3 = 0.05 \text{ g}\mu\text{m}^3/\text{s}^2$. In (a), we consider two different bending moduli $a = 0.005 \text{ g}\mu\text{m}^3/\text{s}^2$ and $a = 0.01 \text{ g}\mu\text{m}^3/\text{s}^2$ with the filament length being fixed

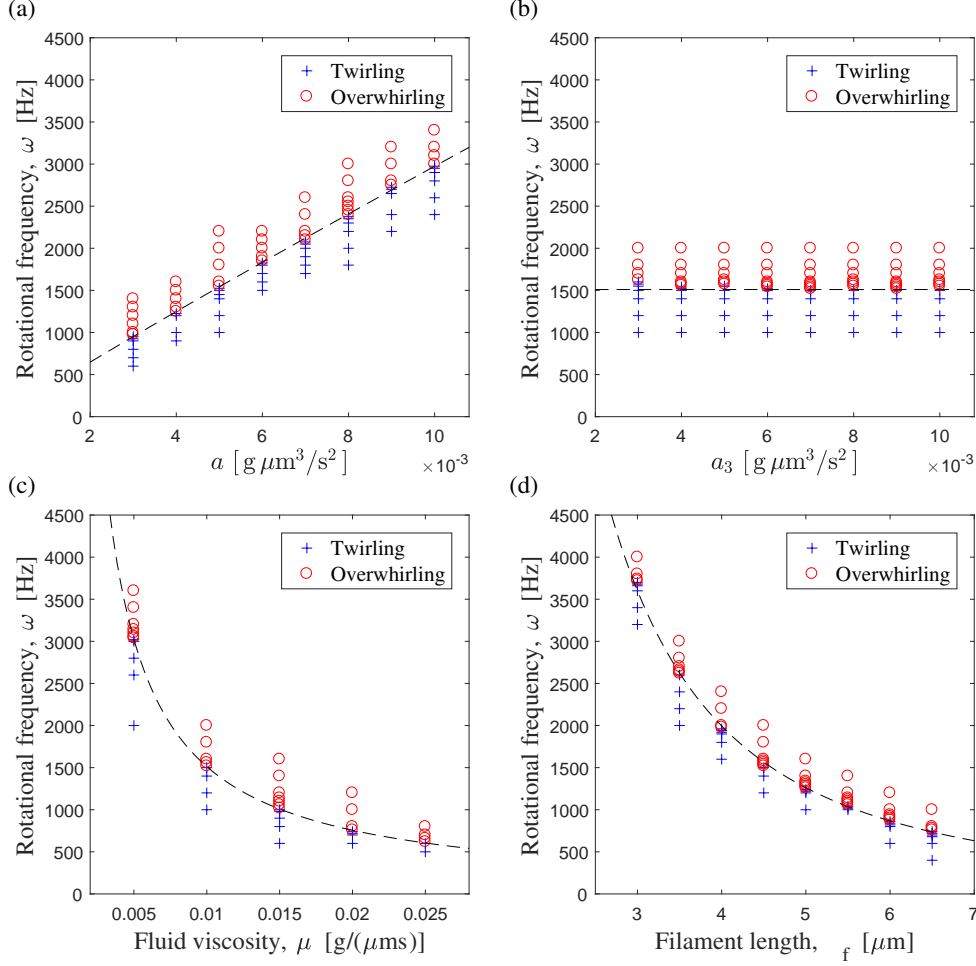


FIG. 3. (Color online) The dynamical states of the rotating filament for various (a) bending modulus of the filament, (b) twist modulus of the filament, (c) fluid viscosity, and (d) the filament length. Red circles represent stable overwhirling motions, and blue crosses represent stable twirling motions. The dashed lines indicate the best fit of the critical frequency ω_c to a function of the form $y = cx^m$.

at $L_f = 4.5 \mu\text{m}$. Next in (b), we vary the filament length $L_f = 4.5 \mu\text{m}$, $5.5 \mu\text{m}$, and $6.5 \mu\text{m}$ with the bending modulus being $a = 0.005 \text{ g}\mu\text{m}^3/\text{s}^2$. For various bending moduli and filament lengths, the critical frequency ω_c decreases as the helical radius r_0 of the filament increases. In fact, we find that ω_c is approximately proportional to $r_0^{-0.4}$ in all the cases considered here, see the dashed lines which indicate the best fit of the critical frequency ω_c to a function of the form $\omega_c = cr_0^m$, where c and m are obtained by the method of least squares.

Fig. 5 shows a subcritical bifurcation diagram resulted from the simulations. The gray area refers to stable twirling state and the white area refers to stable overwhirling state. HB stands for a Hopf bifurcation point at which a stable twirling state is changed into an unstable twirling state.

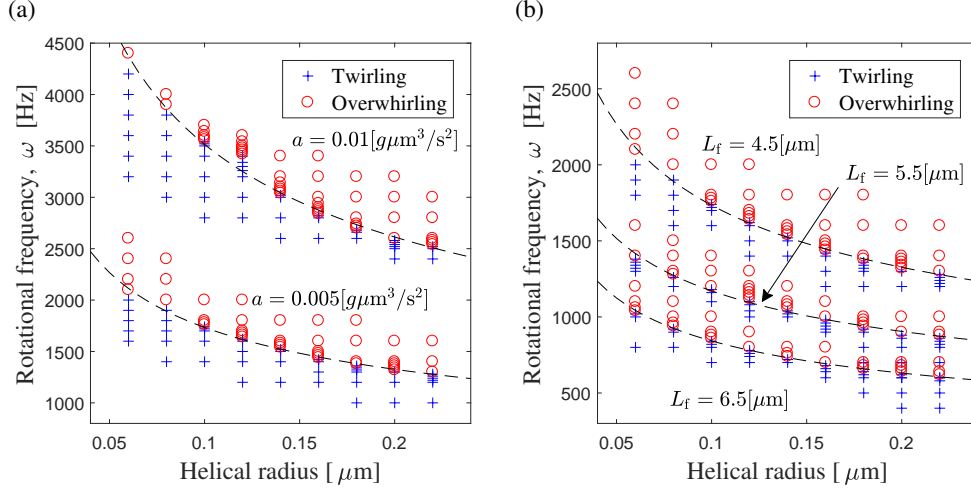


FIG. 4. (Color online) The dynamical states of the rotating filament as functions of the helical radius. We choose two different bending moduli with a fixed filament length in (a) and three different filament lengths with a fixed bending modulus in (b). The helical pitch and the twist modulus are fixed at $2\pi p$ with $p = 1.5 \mu\text{m}$ and $a_3 = 0.05 \text{ g}\mu\text{m}^3/\text{s}^2$, respectively. Red circles represent overwhirling motions, and blue crosses represent twirling motions. The dashed lines are best fitted to a function, $\omega_c \sim r_0^{-0.4}$, where r_0 is the helical radius.

CF stands for a cyclic fold where stable overwhirling and unstable whirling states coalesce. These two bifurcation points determine a bistable region of the two stable states which is the region enclosed by the two vertical dotted lines. Within the bistable region, the helical rod goes to a stable twirling state when the initial tilt of the rod is small; however, the rod approaches a stable overwhirling state when the rod is initially tilted with a large degree. Here the degree of the initial tilt is the mean curvature of the helical axis of the initial flagellum. Thus the open circles which separates the bistable region indicate the dependence of the critical frequency ω_c on the degree of the initial tilt of the rod. The filled circles are representative simulations that induce stable overwhirling state.

B. Buckling instability of a compliant hook

V. alginolyticus is a single-flagellated bacterium of which the flagellum is a left-handed helical filament with its bottom end linked to a short flexible hook. The rotation of the hook and the flagellum is driven by a rotary motor which is embedded into the cell surface [3, 17]. The

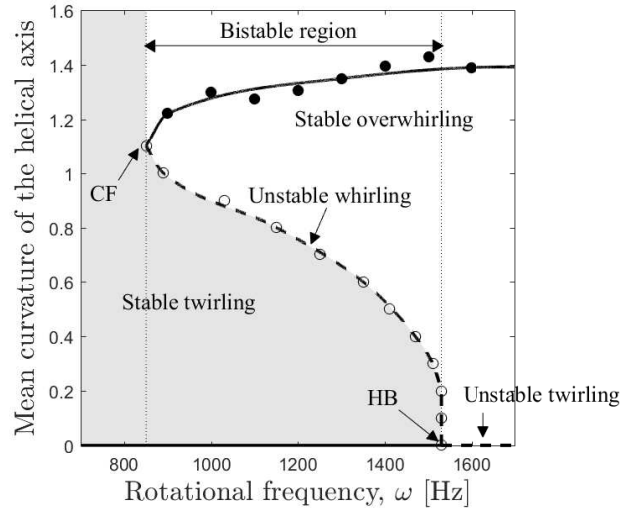


FIG. 5. Subcritical bifurcation diagram. The gray area refers to stable twirling state and the white area refers to stable overwhirling state. The solid lines represent the stable states and the dashed lines represent the unstable states. In the region between the two vertical dotted lines which is determined by HB (bifurcation point) and CF (cyclic fold), the helical rod is in the bistable states separated by the dashed curve which corresponds to the unstable whirling state. The empty circles in the bistable region that are obtained from simulations indicate the critical values of motor frequency and the initial mean curvature of the axis of the helical filament. The filled circles are representative simulations that induce stable overwhirling state.

typical rotational frequency of the motor is approximately 571 ± 12 Hz [18]. The flagellum of the bacterium is covered by a sheath that prevents the filament from transforming [19, 20]. This persistence of the helical handedness of the filament allows the single-flagellated bacterial cell to swim unidirectionally, either backward with CW rotation or forward with CCW rotation in a straight line [21] unless the flagellum bends and flicks the cell body .

Buckling of the hook plays a significant role in determining the swimming pattern and the chemotaxis of single-flagellated bacteria. *V. alginolyticus* swims backward by turning the motor CW while the hook is under tension. Then it suddenly changes the rotational direction of the motor to CCW, which induces the bacterium to swim forward and its hook to be in a compressed state. This state of the hook is called *relaxed* where the hook is unloaded and leads to its buckling followed by the flick of the cell. After the bacterial cell flicks, the hook is under load and becomes stiffer again, which is called a *loaded* state, leading to the steady forward swimming. In the

two different states, the hook takes two different values of the bending modulus while the twist modulus of the hook remains the same. Note that the bending modulus of the loaded hook is always larger than that of the relaxed hook and that the shear and stretch moduli are the same as those of the helical filament.

First we determine the bending and twist moduli of the filament that preserves the intrinsic geometry, namely the helical radius and pitch, even during the rotational motion of the filament. It is known that the flagellar filament of *V. alginolyticus* does not undergo chiral transformation during locomotion [9, 17], which implies that the flagellar filament keeps its helical shape to be left-handed at all times. We fix the rotational frequency at 570 Hz [18], and the intrinsic helical radius and pitch at $0.14 \mu\text{m}$ and $1.49 \mu\text{m}$, respectively [9, 22]. We have varied the values of the twist and bending moduli from $0.01 \text{ g}\mu\text{m}^3/\text{s}^2$ to $0.08 \text{ g}\mu\text{m}^3/\text{s}^2$ and found that the value of $0.05 \text{ g}\mu\text{m}^3/\text{s}^2$ retains the intrinsic property of the helical filament to within 2.5%, and hence we choose this value to be our default value. Note that, in the previous studies [3, 23], bending modulus of the helical filament of *V. alginolyticus* is assumed to be on the order of 10^{-2} .

Fig. 6 illustrates the time evolution of the exemplary dynamical motion of a helical flagellum of *V. alginolyticus* and its corresponding buckling angle when the motor is anchored in space and rotates at the rate of 570 Hz [18]. The buckling angle is defined as the angle between the rotational axis and the helical axis which may subsequently affect the reorientation of the cell. The motor initially turns CW and then reverses to CCW at time $t = 0.06 \text{ s}$. The bending modulus of the hook alternates between two values depending on the states. For the loaded hook, the bending modulus is given as $a_{\text{load}} = 11 \times 10^{-4} \text{ g}\mu\text{m}^3/\text{s}^2$, and for the relaxed hook, the bending modulus is given as $a_{\text{relax}} = 2 \times 10^{-4} \text{ g}\mu\text{m}^3/\text{s}^2$. We draw the trails of some fluid markers (red) which are spread initially around the flagellum to see the direction of the fluid velocity.

In the loaded state in which the motor turns CW, the wave propagates down toward the motor and pumps the fluid downward, see the fluid markers in Fig. 6(a)-(b). In the relaxed mode in which the motor turns CCW, the hook buckles and hence the filament moves away from the axis of rotation, see Fig. 6(c). Once the hook becomes stiff again in the second loaded state, the filament returns back to the original straight state and may lead to forward swimming, which means that the wave propagates from the motor to the proximal end and pumps the fluid upward during CCW rotation, see the fluid markers in Fig. 6(d)-(e). We can clearly see the occurrence of the buckling instability from (c) and the bottom panel of Fig. 6.

In order to explore the effect of the elastic moduli and the length of the hook on the buckling

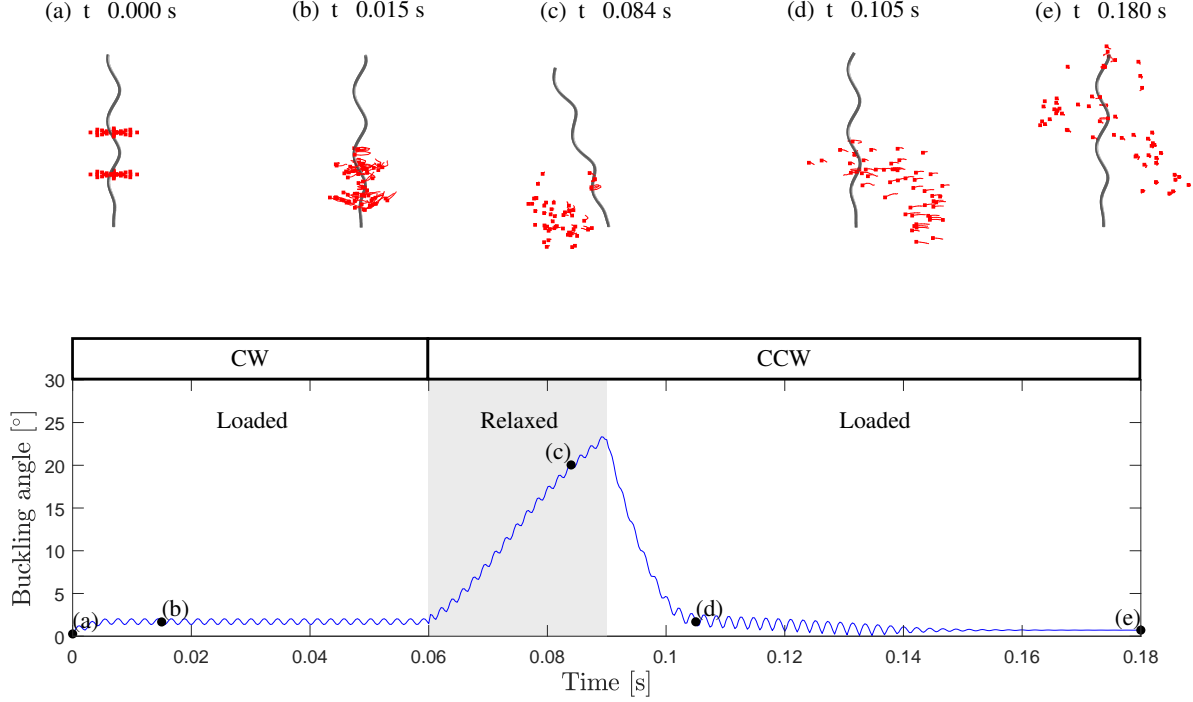


FIG. 6. (Color online) Dynamical motion of a rotating helical flagellum of *V. alginolyticus* (top) and its corresponding buckling angle (bottom) when the motor is tethered in space. The angular frequency of the motor is set to be 570 Hz. The motor initially turns CW and then switches to CCW at $t = 0.06$ s. The bending moduli of the hook in relaxed and loaded states are given as $a_{\text{relax}} = 2 \times 10^{-4} \text{ g}\mu\text{m}^3/\text{s}^2$ and $a_{\text{load}} = 11 \times 10^{-4} \text{ g}\mu\text{m}^3/\text{s}^2$, respectively.

dynamics, we focus on the dynamics of the flagellum right after the motor begins to spin CCW in the relaxed state. While the motor continuously turns CCW at the rate of 570 Hz, the hook is in the relaxed state from $t = 0$ to $t = 0.03$ s and then becomes stiff from $t = 0.03$ in the loaded state. In general, the filament goes through the buckling instability in the relaxed state of the hook when the buckling angle increases. Then the buckling angle decreases in the loaded state when the filament moves toward the axis of the rotation, see Fig. 6.

Fig. 7 shows the time evolution of buckling angles for various bending moduli of the hook as the hook is in the relaxed state followed by the loaded state. The bending modulus of the loaded hook varies while that of the relaxed hook is fixed at $a_{\text{relax}} = 2 \times 10^{-4} \text{ g}\mu\text{m}^3/\text{s}^2$ in the left panel (a), and the bending modulus of the relaxed hook varies while that of the loaded hook is fixed at $a_{\text{load}} = 11 \times 10^{-4} \text{ g}\mu\text{m}^3/\text{s}^2$ in the middle panel (b). We can see that the maximum buckling angle does not depend on the bending modulus of the loaded hook (a), but solely depend on that of the

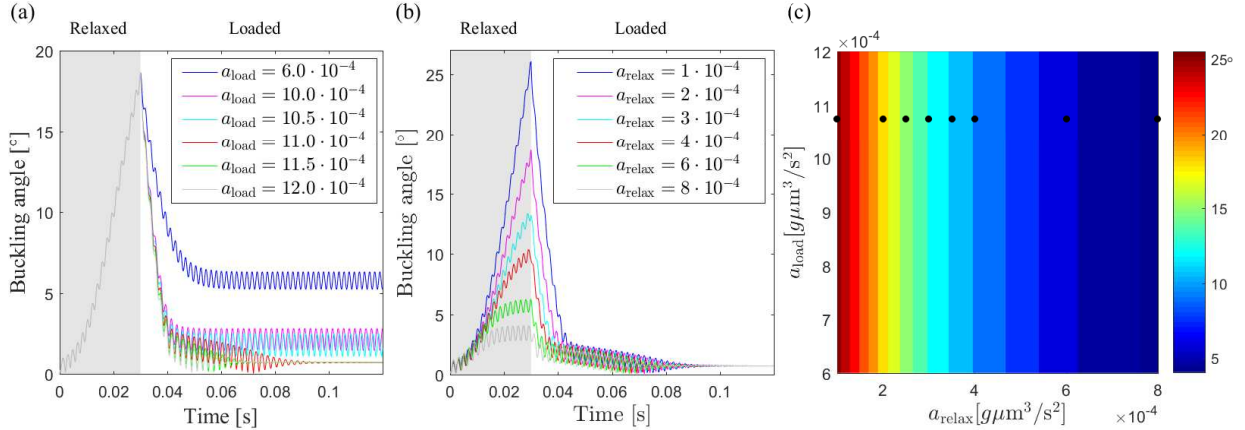


FIG. 7. (Color online) Buckling angles with various bending moduli of the hook. The first two panels show the time evolution of the buckling angle of the hook for various bend moduli when the bending modulus of the relaxed hook is fixed as $a_{\text{relax}} = 2 \times 10^{-4} \text{ g}\mu\text{m}^3/\text{s}^2$ (left) and when the bending modulus of the loaded hook is fixed as $a_{\text{load}} = 11 \times 10^{-4} \text{ g}\mu\text{m}^3/\text{s}^2$ (middle). Right panel illustrates the maximum angle of the buckled hook with various pairs of relaxed and loaded bending moduli. The filled circles indicate the threshold whether or not the buckled hook comes back toward the straight state within 1° .

relaxed hook (b). In fact, the maximum buckling angle is inversely proportional to the bending modulus of the relaxed hook, which is also confirmed in Fig. 7(c) which displays the maximum buckling angle for various bending moduli of the loaded and relaxed states of the hook. As shown in [3], our simulation results confirm that the bending stiffness of the relaxed hook plays a key role in the buckling instability and the determination of a new swimming direction.

Whereas the bending modulus of the relaxed hook is solely related to the maximum buckling angle and thus the reorientation of swimming direction, the bending modulus of the loaded hook also plays an important role in the restoration of the buckling angle. When the bending modulus of the loaded hook is too small, the hook does not go back to the state of the zero buckling angle as shown in Fig. 7(a). We find that there is a threshold for the loaded bending modulus, above which the axis of the helical filament returns back to be aligned to the rotational axis with the deviation being less than 1° . Fig. 7(c) shows the threshold of the loaded bending modulus indicated by the filled circles which is independent of the relaxed bending modulus of the hook.

We also investigate the effect of the twist modulus and the length of the hook on the buckling

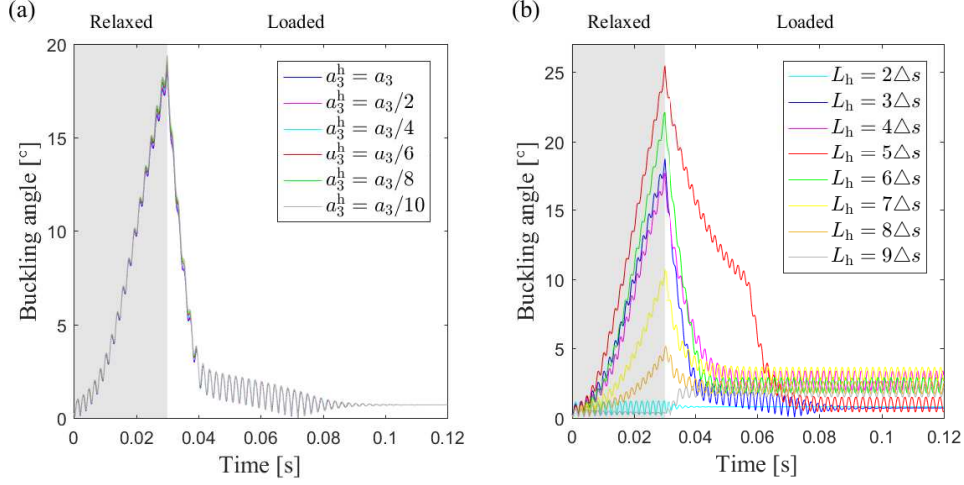


FIG. 8. (Color online) Time evolution of buckling angles for various twist moduli of the hook (a) and hook lengths (b). The bend moduli of the relaxed hook and loaded hook are fixed at $a_{\text{relax}} = 2 \times 10^{-4} \text{ g}\mu\text{m}^3/\text{s}^2$ and $a_{\text{load}} = 11 \times 10^{-4} \text{ g}\mu\text{m}^3/\text{s}^2$, respectively. The twist modulus of the hook in the right panel is $a_3^{\text{hook}} = 0.05 \text{ g}\mu\text{m}^3/\text{s}^2$.

dynamics. While the bend moduli of the hook in the two different states are fixed as $a_{\text{relax}} = 2 \times 10^{-4} \text{ g}\mu\text{m}^3/\text{s}^2$ and $a_{\text{load}} = 11 \times 10^{-4} \text{ g}\mu\text{m}^3/\text{s}^2$, we vary the twist modulus of the hook a_3^{hook} to be $1 \sim 10$ times smaller than that of the helical filament given in Table I. Fig. 8(a) shows the time evolution of the buckling angle for various twist moduli of the hook as the hook is initially in the relaxed state and then later in the loaded state. It is shown in Fig. 8(a) that the buckling angle is independent of the twist modulus of the hook.

Unlike the twist modulus of the hook, the length of the hook substantially affects the buckling angle, see Fig. 8(b) which shows the time evolution of buckling angles for various lengths of the hook. Here the bending moduli of the hook is the same as in Fig. 8(a) and the twist modulus of the hook is given as $a_3^{\text{hook}} = 0.05 \text{ g}\mu\text{m}^3/\text{s}^2$. For small values of the hook length from $L_h = 3\Delta s$ to $L_h = 6\Delta s$, the maximum buckling angles range from 18° to 25° , and the optimal buckling angle is achieved at $L_h = 5\Delta s$. When the hook length L_h is smaller than $3\Delta s$, the maximum buckling angle is almost zero, i.e., buckling instability does not occur, see the case of $L_h = 2\Delta s$ in Fig. 8(b). This is because a shorter rod needs a larger load for the buckling instability, which is implied by Euler's column formula. Note that a typical hook is approximately 100 nm long which

corresponds to around $3\Delta s$ in our case.

As the hook length increases further from $L_h = 7\Delta s$ to $13\Delta s$, a longer hook buckles more readily as predicted in Euler beam theory [3, 24]. However, the maximum buckling angle rapidly drops to be close to zero, see Fig. 8(b). This is because the longer hooks collapse easily to form a flattened S-shape or a loop so that the buckled hook is aligned with the filament axis that remains close to its original rotational axis. This implies that, even though a long hook can easily buckle, it may have no influence on the reorientation of swimming direction.

IV. SUMMARY AND CONCLUSIONS

We have investigated the dynamics of the helical flagellum by adopting the Kirchhoff rod theory combined with the regularized Stokes formulation which governs the surrounding fluid. When a motor at the bottom end of the rod is tethered at a point in space and rotates at a given frequency, we have observed two stable dynamical states, twirling and overwhirling, depending on the angular frequency of the motor and the initial perturbation of the helical axis. A low angular frequency of the motor leads to the stable twirling motion of the helical rod. As the angular frequency of the motor increases to a certain range, the rod resides in a bistable region, taking either twirling or overwhirling motions depending on the initial perturbation from the straight axis of the helical rod. For a sufficiently large rotational rate, the helical rod takes the stable overwhirling motion only. The critical frequency of the transition from the twirling motion and overwhirling one depends on the elastic and geometrical properties of the helical rod and the fluid viscosity, which confirms the theory in literature. The subcritical feature of the bifurcation diagram still remains independent of the physical properties.

We have also observed that the helical rod with a compliant hook experiences buckling instability when the motor switches the direction of rotation and the elastic properties of the hook change. We have found that the buckling angle, which affects the reorientation of the cell body, depends substantially on the bending modulus and the length of the hook, but is independent of the twist modulus. Here we have investigated the role of the hook that may determine the swimming pattern of single-flagellated bacteria by looking at the buckling angle. However, the helical flagellum in our model is fixed in space without a cell body. A more comprehensive study on the role of the hook requires the motion of the cell body to which the flagellum is attached, which will be considered in future work.

ACKNOWLEDGMENTS

Kim was supported by National Research Foundation of Korea Grant funded by the Korean Government (Grant No. 2015R1A2A2A01005420). Lim was supported by National Science Foundation (Grant No. DMS-1410886) and the Charles Phelps Taft Research Center at University of Cincinnati, USA.

-
- [1] H. C. Berg, The rotary motor of bacterial flagella, *Biochemistry* **72**, 1 (2003).
 - [2] R. M. Macnab, in *Escherichia coli and Salmonella typhimurium*, ASM Press, Washington, DC, (1996).
 - [3] K. Son, J. S. Guasto, and R. Stocker, Bacteria can exploit a flagellar buckling instability to change direction, *Nature Physics* **9**, 8, (2013).
 - [4] C. W. Wolgemuth, T. R. Powers, and R. E. Goldstein, Twirling and whirling: Viscous dynamics of rotating elastic filaments, *Phys. Rev. Lett.* **84**, 7 (2000).
 - [5] S. Lim and C. S. Peskin, Simulations of the whirling instability by the immersed boundary method, *SIAM J. on Scientific Computing* **25**, 6 (2004).
 - [6] W. Lee, Y. Kim, S. D. Olson, S. Lim, Nonlinear dynamics of a rotating elastic rod in a viscous fluid, *Phys. Rev. E* **90**, (2014).
 - [7] M. Manghi, X. Schlagberger, and R.R. Netz, Propulsion with a Rotating Elastic Nanorod, *Phys. Rev. Lett.* **96**, 068101 (2006)
 - [8] H. Wada and R. R. Netz, Non-equilibrium hydrodynamics of a rotating filament, *Europhys. Lett.* **75**, 4 (2006).
 - [9] L. Xie, T. Altindal, S. Chattopadhyay, and X. L. Wu, Bacterial flagellum as a propeller and as a rudder for efficient chemotaxis, *Proc. Natl. Acad. Sci. USA* **108**, 6 (2011).
 - [10] M. Koike, H. Terashima, S. Kojima, and M. Homma, Isolation of basal bodies with C-ring components from the Na⁺-driven flagellar motor of *Vibrio alginolyticus*, *J. Bact.* **192**, 375-378 (2010).
 - [11] A. Sen, R. K. Nandy, and A. N. Ghosh, Elasticity of flagellar hooks, *J. of Electron Microscopy* **53**, 3 (2013).
 - [12] T. S. Flynn and J. Ma, Theoretical analysis of twist/bend ratio and mechanical moduli of bacterial flagellar hook and filament, *Biophys. J.* **86**, (2004).
 - [13] R. Cortez, The method of regularized stokeslets, *SIAM J. on Scientific Computing* **23**, 4 (2001).

- [14] S. Olson, S. Lim, and R. Cortez, Modeling the dynamics of an elastic rod with intrinsic curvature and twist using a regularized Stokes formulation, *J. Comput. Phys.* **238** (2013).
- [15] J. J. Higdon, The hydrodynamics of flagellar propulsion: Helical waves, *J. Fluid Mech.* **94**, 331-351 (1979).
- [16] S. Lim, A. Ferent, X. S. Wang, and C. S. Peskin, Dynamics of a closed rod with twist and bend in fluid, *SIAM J. on Scientific Computing* **31**, 1 (2008).
- [17] I. Kawagishi, Y. Maekawa, T. Atsumi, M. Homma, and Y. Imae, Isolation of the polar and lateral flagellum-defective mutants in *Vibrio alginolyticus* and identification of their flagellar driving energy sources, *J. Bact.* **177**, 17 (1995).
- [18] S. Chattopadhyay, and X. L. Wu, The effect of long-range hydrodynamic interaction on the swimming of a single bacterium, *Biophys. J.* **96**, (2009).
- [19] T. Goto, K. Nakata, K. Baba, M. Nishimura, and Y. Magariyama A fluid-dynamic interpretation of the asymmetric motion of singly flagellated bacteria swimming close to a boundary, *Biophys. J.* **89**, (2005).
- [20] M. Furuno, T. Atsumi, T. Yamada, S. Kojima, N. Nishioka, I. Kawagishi, and M. Homma, Characterization of polar-flagellar-length mutants in *Vibrio alginolyticus*, *Microbiology* **143**, (1997).
- [21] S. Lim and C. S. Peskin, Fluid-mechanical interaction of flexible bacterial flagella by the immersed boundary method, *Phys. Rev. E* **85**, 3 (2012).
- [22] Y. Magariyama, S. Sugiyama, K. Muramoto, I. Kawagishi, Y. Imae, and S. Kudo, Simultaneous measurement of bacterial flagellar rotation rate and swimming speed, *Biophys. J.* **69**, (1995).
- [23] Y. Takano, K. Yoshida, S. Kudo, M. Nishitoba, and Y. Magariyama, Analysis of small deformation of helical flagellum of swimming *Vibrio alginolyticus*, *JSME. Int. J.* **46**, 4 (2003).
- [24] Timoshenko, S. *Theory of Elastic Stability* 2nd edn (McGraw-Hill, 1961).